

# Compare the Pair: Rotated vs. Unrotated Surface Codes at Equal Logical Error Rates

Anthony Ryan O'Rourke\*

*Centre for Quantum Software and Information, University of Technology Sydney, Sydney, NSW, 2007, Australia*

Simon Devitt

*Centre for Quantum Software and Information, University of Technology Sydney, Sydney, NSW, 2007, Australia and  
InstituteQ, Aalto University, 02150 Espoo, Finland.*

Practical quantum computers will require resource-efficient error-correcting codes. The rotated surface code uses approximately half the number of qubits as the unrotated surface code to create a logical qubit with the same error-correcting distance. However, instead of distance, a more useful qubit-saving metric would be based on logical error suppression. In this work we compare the number of qubits used by each code to achieve equal logical error rates under circuit-level noise. We perform Monte Carlo sampling of memory experiment circuits with all valid CNOT orders, using the stabiliser simulator Stim and the uncorrelated minimum-weight perfect-matching decoder PyMatching 2. We clarify the well-below-threshold scaling of logical to physical error rates for high odd and even code distances. We find that the rotated code uses  $\sim 74\%$  the number of qubits used by the unrotated code to achieve a logical error rate of  $p_L = 10^{-12}$  at the operational physical error rate of  $p = 10^{-3}$ . The ratio remains  $\sim 75\%$  for physical error rates within a factor of two of  $p = 10^{-3}$  for all useful logical error rates. Our work clarifies the qubit savings provided by the rotated code and provides numerical justification for its use in future implementations of the surface code.

## I. INTRODUCTION

Certain algorithms can be run on quantum computers with far lower processing time and resource requirements than on classical computers [1, 2]. Noise processes impeding this quantum advantage can come from unwanted environmental interactions and the analogue nature of quantum operations. To reliably implement a quantum algorithm requires *fault tolerant* [3, 4] quantum operations and a quantum error-correcting code (QECC), which is a set of quantum states that enable the detection and correction of errors [5]. This involves encoding a qubit as a *logical qubit* of the QECC.

Minimising the resources required to create a QECC is key to realising a scalable, fault-tolerant quantum computer. Such a computer is achievable in theory if the physical qubits which make up its logical qubits experience only finitely correlated errors occurring below some probability threshold.

The surface code [6] is a stabiliser code [3] which has one of the highest thresholds of any quantum code [7] and which was used in an experiment demonstrating that increasing the size of a logical qubit decreases its logical error rate ( $p_L$ ) [8]. This experiment used the *rotated* surface code [9, 10], which uses about half the number of physical qubits as the *unrotated* surface code [11] to create a logical qubit of the same error-correcting distance. However, while the distance achieved is equal, the rate of logical error suppression under uniform depolarising noise is not. For the same distance, the unrotated code outperforms the rotated, achieving a lower  $p_L$  [12, 13] and slightly higher threshold [14]. This is likely because

it features fewer minimum-weight paths that form logical errors (as shown in Fig. 4) [14].

The aim of our work is to provide numerical justification for the use of either the rotated or unrotated surface code by simulating memory experiments and comparing their respective  $p_L$  values under *circuit-level* noise, which assumes every quantum operation can be faulty. We quantify the qubit saving that the rotated code provides not in achieving the same distance as the unrotated code, but in achieving the same  $p_L$ . This is then translated to the number of qubits required to achieve quantum memories of useful lifetimes. Due to its relevance to circuit-level noise, our work also compares the effect of varying the CNOT orders in the stabiliser measurement circuits.

In Section II we provide a background to quantum error correction, the unrotated and rotated surface codes, the order of two-qubit gates in stabiliser measurement circuits and a review of prior work leading to ours. Section III describes our methods. We present and discuss our results in Section IV before concluding in Section V.

## II. BACKGROUND

### A. The surface code

The surface code is a topological stabiliser QECC [3]. It was first introduced as the toric code [6], then with boundaries as the unrotated (planar) surface code [11]. Subsequently it was reformulated as the rotated surface code [9, 10], which only requires about half the number of qubits as the unrotated code for the same distance. Qubit counts for the rotated and unrotated codes are presented in Table I.

The basis states of the surface code's logical qubit are

\* anthony.ourourke@student.uts.edu.au

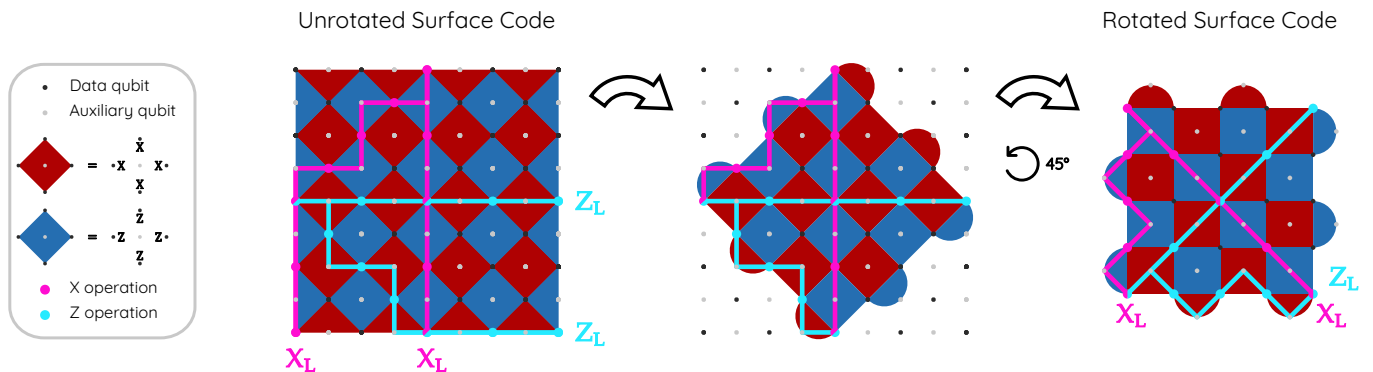


FIG. 1. A  $d = 5$ , unrotated surface code logical qubit and its conceptual rotation to its rotated equivalent. Stabiliser measurements are performed using auxiliary qubits. A single qubit error is visualised as a chain linking the two auxiliary qubits of stabilisers it anti-commutes with, creating a *detection*. Multiple errors form chains that only anti-commute with stabilisers at their endpoints, unless they terminate at a boundary in which case they are undetected. A logical operator  $X_L$  ( $Z_L$ ) is any chain that links boundaries of X(Z)-type boundaries. This requires at least  $d$  X (Z) operations.

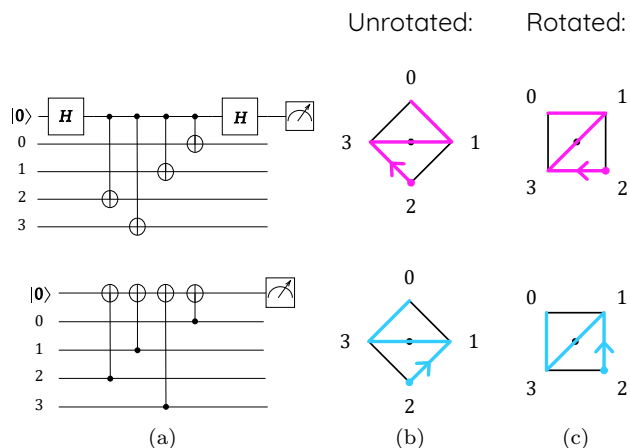


FIG. 2. Representations of X-type (upper diagrams) and Z-type (lower diagrams) stabiliser measurement circuits. The uppermost qubit in each circuit in Subfigure (a) is the auxiliary. Data qubits are numbered from 0 to 3 depending on their position relative to the auxiliary in the surface code lattice, as depicted in (b) and (c) where the auxiliary is at the centre of the stabiliser it measures. We refer to the depicted CNOT order as 23102130, quoting X then Z-type order.

superpositions of entangled *data qubits*. The minimum number of single-qubit operations required to transform from one basis state to the other is the *distance*  $d$ . This is a logical operation, or logical error if unintended, and cannot be detected by the code. Continuous noise on qubits is discretised in stabiliser codes such as the surface code by projective measurements of the code *stabilisers* [3]. Stabilisers are usually tensor products of the Pauli operators  $\mathbb{1}$ ,  $X$ ,  $Y$  and  $Z$  and are unitary and Hermitian operators whose  $\pm 1$  measurement outcomes do not depend on the state itself but on which errors have occurred. Consequently, measuring the stabilisers does not destroy information in the logical state, but discre-

tises the noise and projects the state to an eigenstate of the stabilisers. *Auxiliary qubits* are used to perform and report the outcomes of stabiliser measurements, also referred to as a syndrome. The un-errored state of a logical qubit is a superposition of the joint  $+1$  eigenstates of the code stabilisers.

Fig. 1 depicts a distance-5 unrotated surface code logical qubit and its conceptual rotation to form its rotated equivalent.  $Z$  ( $X$ ) errors anti-commute with X(Z)-type stabilisers to give  $-1$  measurement outcomes, or *detections*. Single-qubit errors are visualised as linking auxiliary qubits of the stabilisers they anti-commute with and can hence be detected by. Multiple errors form chains which only anti-commute with stabilisers at their endpoints, unless they terminate at a boundary in which case they are undetected. Logical Pauli operations are generated by  $X_L$  and  $Z_L$ , which mutually anti-commute but commute with the stabilisers.  $X_L$  ( $Z_L$ ) is a chain of at least  $d$  X (Z) operations which terminates at opposite boundaries of X(Z)-type stabilisers.

	Unrotated	Rotated
Data qubits	$2d^2 - 2d + 1$	$d^2$
Auxiliaries	$2d^2 - 2d$	$d^2 - 1$
Total qubits	$4d^2 - 4d + 1$	$2d^2 - 1$

TABLE I. A distance- $d$  logical qubit's physical qubit count.

## B. Errors and decoding

QECCs such as the surface code aim to protect the information stored in their logical qubits even as their physical qubits experience noise. The stabiliser generators are used to discretise and detect errors. They are measured using the circuits in Fig. 2(a). Each stabiliser generator has its own measurement circuit. The X(Z)-type circuit is in the upper (lower) half of the figure. In-

cluding initialisation and measurement of the auxiliary, the circuit’s depth is eight (six). If idling errors with the same error probabilities as the Hadamard gates are inserted in the Z-type measurement circuit to correspond to the idling time while the Hadamards are applied in the X-type circuit, then the effect on the logical error rate is that the circuits are of effectively equal depth.

The initialisation of the auxiliary and each of the gates in the stabiliser measurement circuits can be faulty, however a *code capacity* noise model assumes they are not. In it, errors are modelled only on data qubits and precede perfect syndrome extractions that report correct measurement outcomes. *Circuit-level* noise, on the other hand, models all the gates as faulty, as well as features idling errors which apply to any qubit not being operated in a particular time step, that is while a gate is being applied to another qubit. Uniform depolarising, or standard depolarising, circuit-level noise [7] assumes an equal probability of errors affecting different gates in the circuit, as shown in Table II.

The measurement circuit can consequently cause errors to spread between data and auxiliary qubits, report an incorrect measurement result or both. Performing multiple repetitions, also known as rounds or cycles, of syndrome extraction increases its reliability. When a measurement value changes from the previous round this is a detection event across time. This contrasts to an error on a data qubit which will change the measurement results of the stabiliser generators adjacent to it in space. A single chain of errors can include errors both in space and time. An error syndrome thus exists in a space-time volume.

Errors can be corrected by deriving which pattern of errors reproduces a given syndrome. The difficulty in successfully identifying errors is that multiple patterns of errors can cause the same syndrome and, as a code with  $n$  data qubits usually contains  $O(n)$  stabilisers, the number of syndromes scales as  $2^n$ , rendering a simple look-up table intractable. Solving this problem is known as *decoding*. A decoder must be ‘fast’ enough in solving this problem to avoid an exponentially growing backlog of output from the quantum computer [15, 16] so that subsequent logical operations are performed correctly. Some decoders are highly accurate [17, 18], others are fast [19–25] and some are both [26].

Minimum-weight perfect-matching (MWPM) decoders such as Sparse Blossom [23] are fast and widely used for surface codes. They treat detection events as vertices in a graph connected by edges which represent the physical errors that would trigger those detectors, weighted by their probability of occurring. A perfect matching involves finding a set of errors which would cause the observed error syndrome, and the perfect matching with the minimum weight indicates the most likely set. Fig. 4 shows the X-error matching graphs for the rotated and unrotated surface codes. In this case edges are X errors and nodes are the auxiliary qubits of Z-type stabilisers. The Z-error matching graph would be equivalent but features Z-errors with nodes on X-type stabilisers.

One way to test the error-correcting performance of a QECC and a decoder can be done with Monte Carlo sampling of many *memory experiments*, as in [7, 12, 27]. A memory experiment is also applicable to performing logical operations on logical qubits when using lattice surgery, as it requires preserving a logical qubit in memory but changing the order of stabiliser measurements along its boundaries [9]. A memory experiment in the surface code in the  $Z_L (X_L)$  basis requires encoding the  $|0\rangle_L (|+\rangle_L)$  state by initialising all data qubits to  $|0\rangle (|+\rangle)$  then performing the first round of stabiliser measurements. After preserving the state through more rounds of stabiliser measurements, usually  $d$  [7] or  $3d$  [8, 27, 28], the logical qubit is measured by measuring the data qubits in the Z (X) basis then checking their parity under  $Z_L (X_L)$ . The detection events and measurement results are decoded and the necessary corrections decide whether the measurement result should be flipped or not to interpret the correct result. We refer to this experiment as memory Z (X). A logical error occurs if single-qubit errors on data qubits formed a logical operator during the experiment or if the decoder fails and its suggested corrections form a logical operator.

As long as the physical error rate ( $p$ ) affecting the faulty gates and qubits in the QECC is below a certain probability threshold ( $p_{th}$ ), increasing the distance of the code decreases the logical error rate  $p_L$  [29]. Memory experiments over various  $d$  and  $p$  reveal a code’s threshold for the noise model and decoder.

Below threshold  $p_L$  scales with  $p$  according to the power law

$$p_L = \alpha_1 \left( \frac{p}{p_{th0}} \right)^{d_e} + \alpha_2 \left( \frac{p}{p_{th1}} \right)^{d_e+1} + \alpha_3 \left( \frac{p}{p_{th2}} \right)^{d_e+2} + \dots \quad (1)$$

where the error dimension  $d_e = d/2$  for even code distances and  $d_e = (d+1)/2$  for odd code distances [19, 30]. The reasoning behind this is that  $d_e$  errors aligned along a logical minimum-weight chain will cause the decoder’s corrections to complete the chain, forming a logical error.

The  $p_L$  of a memory experiment is usually reported per  $d$  rounds of stabiliser measurements as this is the number of rounds required for fault-tolerant merge and split operations when using lattice surgery for logical quantum computation [9] and reporting per round would result in an overestimate of the threshold [7].

Although the  $|0\rangle_L (|+\rangle_L)$  state is a +1 eigenstate of  $Z_L (X_L)$  and in the surface code is hence unaffected by single-qubit  $Z (X)$  errors, both types of stabilisers must be measured in a memory experiment to realistically simulate error-mixing introduced by the stabiliser measurements and estimate the code’s performance for an unknown state. For example, the measurement of X-type stabilisers to detect Z errors can copy a single X error to two or more data qubits. While the Z errors would not affect the  $|0\rangle_L$  state, the copied X errors would. Furthermore, when a Y error occurs it creates correlations in the separate X and Z detector graphs. Uncorrelated

decoders [23] treat these as separate  $X$  and  $Z$  errors and assume if a single-qubit error occurs with probability  $p$  then a  $Y$  error occurs with probability  $p^2$ . Correlated decoders have been shown to boost performance [12].

### C. CNOT Order and Hook Errors

The order of the CNOT gates in the stabiliser measurement circuits must be chosen carefully so the stabiliser circuits can be performed in parallel and do not unnecessarily introduce errors. This can be summarised into three criteria which we will now describe. Any CNOT order which satisfies these criteria we refer to as a *valid* CNOT order. To explain the criteria we will use CNOT labelling depicted in Fig. 2, in which the data qubits are numbered clockwise from 0 depending on their position relative to the auxiliary qubit.

1. The CNOT order must ensure stabilisers mutually commute so give deterministic measurement outcomes in the absence of errors [31]. Practically, shared data qubits between two or more stabilisers must be interacted with in the same relative order by their shared stabilisers. That is, if one stabiliser's interaction precedes another for any shared qubit, it must do so for all shared qubits.
2. Unnecessary idling errors can be avoided by ensuring that all CNOTs in a particular time step are physically parallel (aligned along the same axis). Using the labelling of Fig. 2, this implies that while all the X-type stabilisers are measuring data qubits 0 or 2 (1 or 3), the Z-type stabilisers can measure either 0 or 2 (1 or 3).
3. In the rotated surface code, CNOT order should avoid *hook errors* [19, 32] (see explanation below).

A hook error, or *horizontal hook error* [19], is the copying of a single physical error to two data qubits that align with a logical operator. As shown in Fig. 3(a), the X(Z)-type stabiliser measurement circuits can copy  $X$  ( $Z$ ) errors onto data qubits. Copying to four data qubits is equivalent to applying the stabiliser (a logical identity gate) while to three is only a single error up to multiplication by a stabiliser. Copying to two data qubits which align with a logical operator of the same type causes a hook error as the logical operator can now be formed with half as many physical errors as the code distance implies. Fig. 3(b) depicts which two CNOTs result in a hook error for each stabiliser type if they are the final two CNOTs in the stabiliser's measurement circuit. Appendix Fig. A.2 shows the effect of hook errors on the relation between  $p_L$  and  $p$  for the rotated surface code.

In the unrotated code, the copied error cannot align with a logical operator so does not have the same effect. We investigated this as an aside in our simulations and found that half the unrotated orders performed

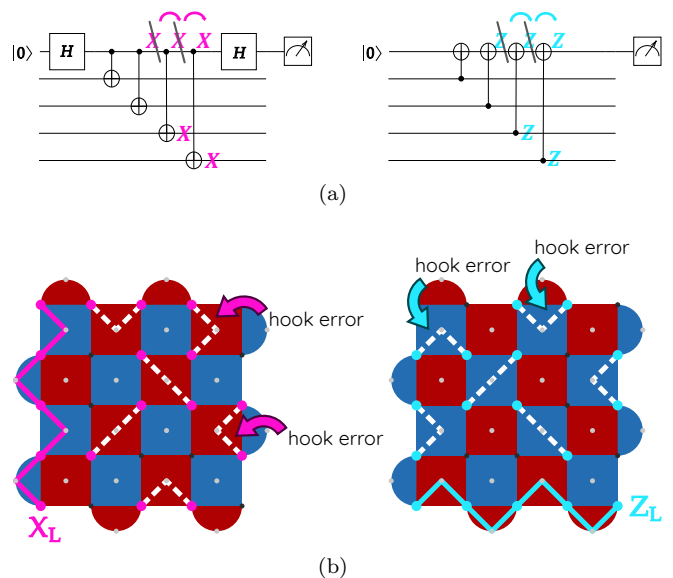


FIG. 3. (a) CNOTs copying an error which precedes them in the syndrome extraction circuits. Up to multiplication by a stabiliser, copying to four data qubits is the identity whereas to three is equivalent to a single error. If the error precedes the two final CNOTs it is copied to two data qubits. The possible orientations of these two qubits are shown in (b). If these align with a logical operator of the same type as the error the logical operator can be formed with half as many single-qubit errors as expected. This is a hook error [19, 32].

marginally better than the other half, however this had no correspondence with orders that create hook errors in the rotated code (see Appendix Fig. A.3).

### D. Prior Work

In this section we review prior work which led to ours, outlining prior threshold values,  $p_{th}$ , for the rotated and unrotated surface code as well as previous work comparing their logical error rates.

Fowler et al. [30] simulated the unrotated code for odd distances. They used a uniform depolarising circuit-level noise model and a MWPM decoder for  $p$  values which corresponded to a  $p_L$  per round of approximately  $10^{-5}$  and found, to first order, that  $p_L$  scales with  $p$  as  $p_L \approx 0.03(p/p_{th})^{d_e}$  where  $d_e = (d-1)/2$ .

For the unrotated surface code, Stephens [7] clarified using numerical simulations how estimates of its threshold depend on noise model, the syndrome extraction circuits and the decoder. As the X-type's measurement circuit (see Fig. 2(a)) is of greater depth, the logical error suppression will be worse and the threshold consequently higher for the memory experiment preserving the  $|0\rangle_L$  state, that is memory  $Z$ . Reporting  $p_L$  per  $d$  rounds and using a MWPM decoder and uniform depolarising circuit-level noise, as defined in Section II B, Stephens found a threshold of  $p_{th} \approx 0.0050$  for memory  $X$  and

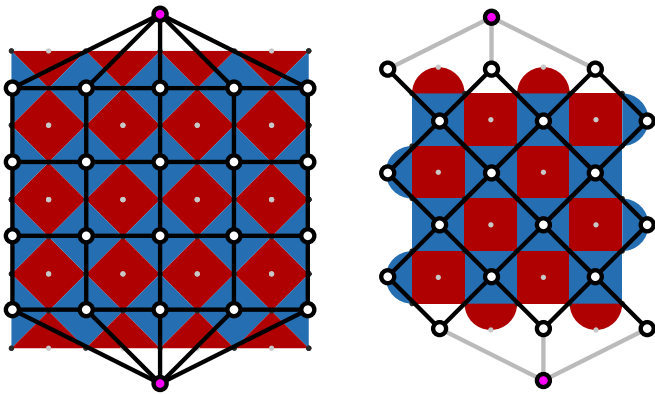


FIG. 4. Graphs for which paths between the two coloured vertices correspond to an  $X_L$  operator on distance-5 surface codes. Fig. adapted from [14]. Left: unrotated surface code, right: rotated surface code, with grey edges costing nothing to traverse. Forming a minimum-weight path in the unrotated surface code cannot be done using horizontal edges. This results in only  $d$  (in this case 5) minimum-weight paths forming a logical error. In the rotated code all the edges can be used, resulting in a lower bound of  $\binom{d}{\lfloor d/2 \rfloor}$  minimum-weight paths [14]. In this case there are 52.

$p_{th} \approx 0.0054$  for memory Z.

Criger and Ashraf [14] compared the rotated and unrotated codes under a code capacity noise model and using a MWPM decoder. The rotated code had a slightly lower threshold than the unrotated. This was suggested as the non-optimal decoder being affected by the different number of minimum-weight paths that can cause logical errors in the two codes. This is depicted in Fig. 4 for  $X_L$ . To form a particular logical operator, a distance- $d$  unrotated code has only  $d$  minimum-weight paths. This arises from the fact that any diversion from a direct path joining boundaries together is no longer a minimum-weight path. For the rotated surface code however, all of the edges can contribute to a minimum-weight path, implying the number of minimum-weight paths is lower bounded by  $\binom{d}{\lfloor d/2 \rfloor}$ , which is much greater than the unrotated code.

Beverland et al. [13] compared the two codes using the code capacity noise model and both analytical and numerical methods. For the same number of qubits, the rotated code can achieve a higher distance than the unrotated code and consequently achieves a lower  $p_L$  at  $p$  values below threshold. That is, except for  $p$  very close to threshold the unrotated code achieves a lower  $p_L$  than the rotated code, even though it is of a lower distance.

Paler and Fowler [12] used uniform depolarising circuit-level noise and a MWPM decoder. They simulated odd code distances from  $d = 3$  to  $d = 9$  with  $p_L$  reported for memory X and showed the unrotated code achieves a lower  $p_L$  per round than the rotated surface code for distance 5, 7 and 9, as simulated for  $p$  values corresponding to a  $p_L$  per round of approximately  $10^{-7}$ . Distance 3 was an exception, but due to being a very low distance code it would suffer *edge effects* in space.

That is, the proportion of low-weight stabilisers (weight-2 in the rotated code, weight-3 in the unrotated) on the boundaries of the surface code lattices as compared to the weight-4 stabilisers in the bulk of the lattice is higher for lower-distance codes and these have a consequent reduction in performance.

Gidney et al. [27] compared the rotated surface code to another QECC [33] to estimate the number of qubits required to reach the *teraquop* regime, which is a  $p_L$  per  $d$  rounds of one in a trillion. This implies that a trillion logical operations (each requiring  $d$  stabiliser measurement rounds) can be performed before, on average, one logical error occurs. Using standard depolarising circuit-level noise (referred to in the paper as SD6), with an uncorrelated MWPM decoder and plotting  $p_L$  per  $d$  rounds they showed the rotated code has  $p_{th} \approx 0.005$ .

These results show that the unrotated code has a slightly higher threshold than the rotated code, as well as achieves a lower  $p_L$  for the same distance when subjected to uniform depolarising noise. In the next section, we detail our methods to address higher code distances, both odd and even, for lower logical rates and under circuit-level noise.

### III. METHODS

In this work we simulated memory experiments in the rotated and unrotated surface code using both odd and even distances, low physical error rates and uniform depolarising circuit-level noise. Our aim was to compare the unrotated and rotated code, quantifying the latter's advantage in terms of the number of qubits used to achieve the same  $p_L$  values and provide evidence that this persists for high  $d$  and low  $p$ . In this comparative study we implemented a uniform depolarising circuit-level noise model, with faulty gates detailed in Table II, and the fast MWPM algorithm Sparse Blossom, implemented in Py-Matching version 2 [23].

Faulty Gate	Description
Idling	An idle qubit experiences either $X$ , $Y$ , or $Z$ , each with probability $p/3$ .
Initialise / reset	Setting a qubit to $ 0\rangle$ ( $ +\rangle$ ) instead prepares $ 1\rangle$ ( $ -\rangle$ ) with probability $p$ .
Hadamard	A Hadamard gate $H$ is followed by $X$ , $Y$ , or $Z$ , each with probability $p/3$ .
Measurement	A measurement in the $X$ or $Z$ basis reports the incorrect result and projects to the orthogonal eigenstate with probability $p$ .
CNOT	A CNOT is followed by a two-qubit operation from the set $\{1X, 1Y, 1Z, X1, XX, XY, XZ, Y1, YX, YY, YZ, Z1, ZX, ZY, ZZ\}$ , each with probability $p/15$ .

TABLE II. Uniform depolarising circuit-level noise.

We performed Monte Carlo sampling of trillions of runs of memory experiments in both codes, run for both mem-

ory X and memory Z. Extending from the qubit count to  $p_L$  ratios will be resource estimates of the required qubit counts for desirable quantum memory times.

Our generated data, as well as the python code used to generate the circuits, run simulations and render plots is available at GitHub repository [github.com/wamud/compare\\_the\\_pair](https://github.com/wamud/compare_the_pair). We used Stim [34], a tool for simulation and analysis of stabiliser circuits; PyMatching 2 [23], a fast MWPM decoder; and Sinter [35], which uses python multiprocessing for bulk sampling and decoding of Stim circuits.

For each code and physical error rate, we generated a Stim circuit file [36] for the stabiliser circuit realising a memory experiment. This file contains annotations to simulate the stabiliser circuit, including the qubits and noisy operations, to assert that the parity of certain measurement sets, i.e. detectors, are deterministic in the absence of noise and to assert which final measurements are combined to calculate the measurement result of the logical observable. The detection events are converted to a hypergraph for PyMatching to decode.

To generate the Stim circuits, we modified Higgott and Le Régent’s [37] python translation of Stim’s [34] in-built function for generating surface code circuits. We enabled the option to exclude detectors in the opposite basis to that of the measured logical observable as these detection events are not used by PyMatching as it is an uncorrelated decoder. We added modifications that enabled the re-ordering CNOT gates, suggested as the explanation for the difference in the unrotated surface code’s  $p_L$  between memory X and memory Z [38], and added idling errors on any qubits not being operated on while gates are being applied to other qubits. This included adding idling errors with the same error probabilities as the Hadamard gate on the auxiliary qubits used to measure Z-type stabilisers while Hadamard gates are applied to the X-type stabiliser auxiliaries. This renders the two syndrome extraction circuits to be effectively of equal depth. For an example of a circuit, Appendix Fig. A.1 depicts a distance-2 surface code circuit implementing a memory Z experiment and displaying our modifications.

To minimise uncertainty in the results we incrementally scaled the maximum number of samples taken of each memory experiment type while correspondingly reducing the maximum number of logical errors seen before sampling would automatically stop. We initiated our simulations with a ceiling of one million shots and one hundred thousand errors, incrementally increasing the shot count to a trillion and tapering down the maximum errors to twenty. This was performed using the software Sinter [35] on two 64-core computers.

We calculated  $p_L$  per  $d$  rounds but ran  $3d$  rounds of stabiliser measurements to reduce time-boundary edge effects, which arise because the first and last round have less logical errors [28]. The  $p_L$  per  $d$  rounds is hence the XOR of three independent Bernoulli distributions.

## IV. RESULTS AND DISCUSSION

### A. Affect of CNOT order

Fig. 5 displays plots of  $p_L$  per  $d$  rounds of stabiliser measurements versus  $p$  from our simulation results. Before discussing our main result, in this section we address the noticeable separation between the unrotated code’s memory X and Z results. This occurred despite the stabiliser measurement circuits (Fig. 2) being effectively of equal depth due to idling errors (see Section III).

If we first consider the rotated code, it had indistinguishable  $p_L$  versus  $p$  for memory X and Z up to uncertainty, as depicted by the ‘X’ and pentagonal markers in Fig. 5 being overlaid. This reproduced for all valid CNOT orders (see Appendix Fig. A.2), which avoid hook errors (results with hook errors also in Appendix Fig. A.2), and was due to the stabiliser measurement circuits in Fig. 2(a) being of effectively equal depth due to idling errors.

On the other hand, the unrotated code had differing memory X and Z performance depending on its CNOT order. To be a valid order the first and last of the four CNOTs align with one minimum-weight logical operator in the unrotated code, while the second and third (‘inner’) CNOTs align with the other. If the inner CNOTs align with the minimum-weight  $Z_L$  operator (so act on data qubits 1 and 3 in Fig. 2(a)) we see a lower  $p_L$  for memory Z, which exactly inverts (see Appendix Fig. A.4) if they align with  $X_L$  (so act on data qubits 0 and 2 in Fig. 2(a)). This was observed for all valid unrotated orders, with an additional, unrelated marginal increase in performance observed for half the orders (see Appendix Fig. A.3). This affect was not artificially introduced from the orientation of the matching graph given to the decoder, as shown in Appendix Fig. A.5 which presents simulations with the stabiliser types inverted.

This alignment of the inner CNOTs correlates with a split in performance but is not causative. If the inner CNOTs increased the occurrence of the logical operator they align with then increasing total circuit depth to enable interspersing of the alignment of all four gates should symmetrise the unrotated code’s performance. This did not occur, as shown in Appendix Fig. A.6. Further investigation was outside the scope of this paper, especially as the unrotated code did not outperform the rotated even when leveraging this effect (see Section IV C).

Usually the worst-case code sets the overall threshold [7], and unless preserving a known Pauli eigenstate, which has limited utility, the CNOT order cannot be chosen to achieve the best-case performance of the unrotated code. Subsequent comparisons hence use an ordering which shows the aforementioned marginal increase in performance but is a worst-case unrotated code for the memory type, featuring a CNOT ordering unfavourable to the preserved state. We will refer to this simply as the unrotated code. For specificity we are reporting  $p_L$  results for memory Z. The orders are rotated order 32013021 and

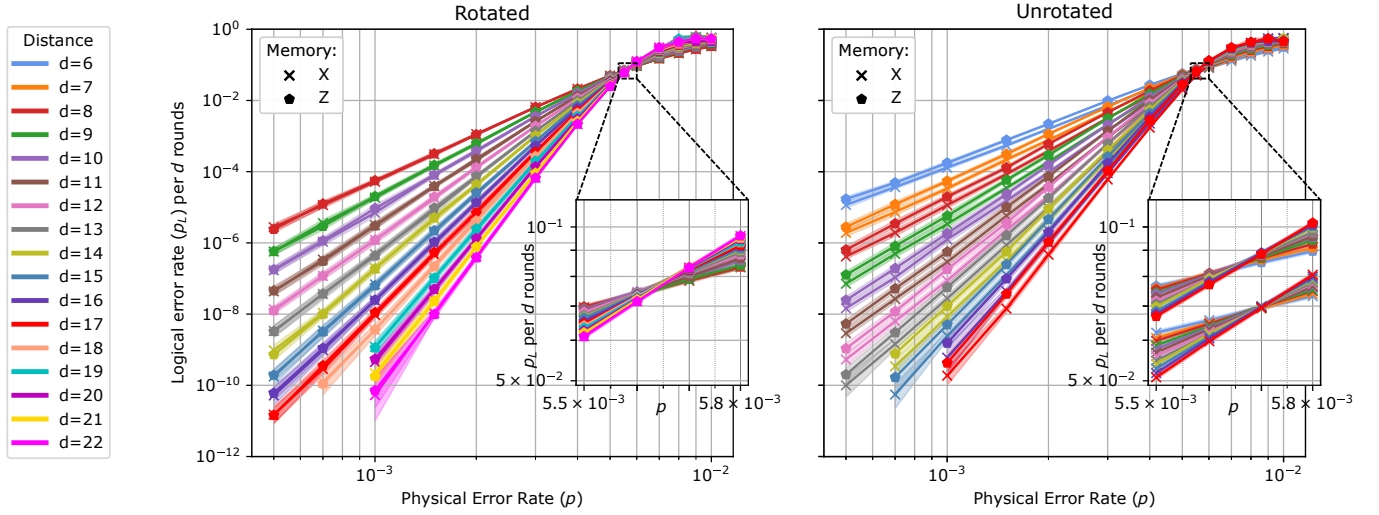


FIG. 5. Logical error rate per  $d$  rounds (cycles) of syndrome extraction vs. the rate of uniform depolarising circuit-level noise. Memory X (Z) preserves the  $|0\rangle_L$  ( $|+\rangle_L$ ) state. The threshold ( $p_{th}$ ) is the  $p$  value where the curves intersect. Insets show a zoomed-in region close to  $p_{th}$  with additional data points. The split between memory types in the unrotated code is discussed in Section IV A. For subsequent comparisons we take its worst case. Displayed results are from CNOT orders rotated 32013021 and unrotated 10231203, numbering as per Fig. 2, but for all valid CNOT orders these results generalise (see Section IV A). With  $k$  logical errors observed, highlighted regions show  $p_L$  values for which the conditional probabilities  $P(p_L|k)$  are within a factor of 1000 of the maximum likelihood estimate (MLE)  $p_L = k/n$ , assuming a binomial distribution and converted to per  $d$  rounds. We ran  $3d$  rounds, with the per  $d$  rounds the XOR of three independent Bernoulli distributions.

unrotated order 10231203 ( $X_L$ -aligned inner CNOTs). However, these results reproduce for memory X (see appendix figures A.2 and A.3) so the exact choice of valid CNOT orders with a worst-case unrotated order is arbitrary.

### B. Logical error rate vs. physical error rate

We now present our results for  $p_L$  to  $p$  scaling for the two codes. The insets in Fig. 5 display zoomed-in regions close to threshold with additional simulated data points. By inspection we find

$$p_{th_{\text{ro}}} \approx 5.64 \times 10^{-3} \quad (2)$$

$$p_{th_{\text{unro}}} \approx 5.66 \times 10^{-3}. \quad (3)$$

Our threshold value for the rotated code is comparable to the  $p_{th} \approx 5 \times 10^{-3}$  value from Gidney et al. [27] who also implemented circuit-level uniform depolarising noise but used an in-house MWPM decoder. We also see a slightly higher threshold for the unrotated code than the rotated, as noted in Ref. [14].

The behaviour for error rates well-below threshold is more applicable to useful quantum computing. Our results show that for a given distance, the unrotated code achieves a lower  $p_L$  than the rotated code. For the same distance, it was previously shown [12] that the unrotated code achieves a lower  $p_L$  than the rotated, investigated using odd  $d$  from 5 to 9 inclusive to a  $p_L$  per round as low as  $\approx 10^{-7}$ . We confirm this pattern continues for

higher odd as well as even distances and down to a  $p_L$  per round of  $\approx 10^{-12}$  (a  $p_L$  per  $d$  rounds  $\approx 10^{-11}$ ).

We now present our results fitting to the scaling relationship between  $p_L$  and  $p$ . Previous results [30] fit to Equation 1, but this was at higher logical error rates. We found that even if including the higher order terms in Equation 1, it failed to capture our data's scaling relationship. We hence instead fit to

$$p_L = \alpha (p/\beta)^{\gamma d - \delta}, \quad (4)$$

where we can define the error dimension  $d_e = \gamma d - \delta$ . Our fits used  $d \geq 6$  (8) for the unrotated (rotated) code to minimise edge effects that prevent low-distance codes from following the same scaling relationship (see Appendix Fig. A.7), and  $p \leq 0.004$  because the scaling of  $p$  values closer to  $p_{th}$  was not indicative of sub-threshold performance. For this reason and to avoid confusion we label the term in the denominator  $\beta$  rather than  $p_{th}$  because it reflects the region of intersection of line-fits based on sub-threshold scaling rather than on simulated data very close to threshold (as in equations 2 and 3).

The performance for odd-distance codes scales better than even-distance codes at low distances (see Appendix Fig. A.7), however when fitting to high distances their scaling relations were identical up to uncertainty. This contrasts with previous results [30] which found significant differences, namely  $d_e = d/2$  for even code distances and  $d_e = (d+1)/2$  for odd code distances. We consequently combined both odd and even distances in the fits

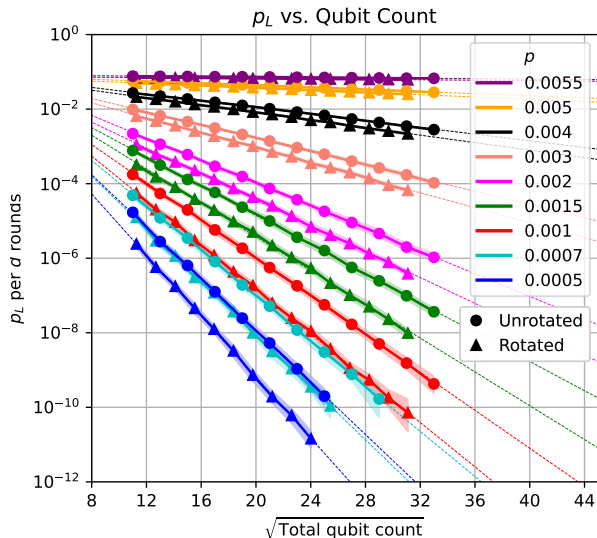


FIG. 6. Line-fit plot showing  $p_L$  as a function of qubit count for the rotated and unrotated surface codes. We fit to  $d \geq 8$  for the rotated and  $d \geq 6$  for the unrotated code to minimise edge effects. The points of intersection between these least-squares line fits and  $p_L = 10^{-12}$  are used to generate the ‘teraquop’ plot in Fig. 8. Highlighted regions show  $p_L$  values for which the conditional probabilities  $P(p_L|k)$  are within a factor of 1000 of the MLE  $p_L = k/n$ , assuming a binomial distribution. These results report memory Z but reproduce up to uncertainty for memory X (see Section IV A).

and found

$$p_{L_{ro}} = 0.078 (p/0.0053)^{0.578d-0.27} \quad (5)$$

$$p_{L_{unro}} = 0.080 (p/0.0054)^{0.700d-0.65} \quad (6)$$

Plots displaying these curve fits superimposed on sampled data can be found in Appendix Fig. A.8, while the parameters and their uncertainties for odd, even and combined odd and even distances can be found in the Appendix in Table III.

### C. Logical error rate vs. qubit count

We now present our main result, which, in short, is that the rotated code uses  $\sim 75\%$  the number of qubits used by the unrotated code to achieve the same logical error rate. We will now detail how we arrived at this value, and note that the exact value depends on the physical and logical error rate.

When using Fig. 5 to compare the codes for roughly the same qubit count, say  $d = 18$  for the rotated code (647 qubits) and  $d = 13$  for the unrotated (651 qubits), we see that the rotated code achieves a lower  $p_L$ . To formalise this we restructure the data, taking slices at each  $p$  value, and plot qubit count vs.  $p_L$  in Fig. 6. We note that the rotated code achieves a lower  $p_L$  than the

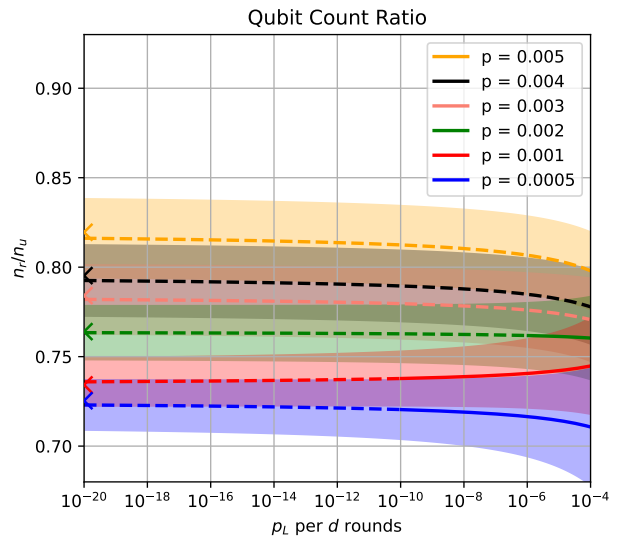


FIG. 7. The ratio of the number of qubits used by the rotated versus the unrotated surface code to achieve the same logical error rate ( $p_L$ ) per  $d$  rounds for a selection of physical error rates ( $p$ ). Qubit counts are calculated from the line-fits of Fig. 6, with projected qubit counts indicated by dashed lines. Coloured arrowheads on the y-axis indicate the limit as  $p_L \rightarrow 0$ . Simulations implemented uniform depolarising circuit-level noise and an uncorrelated MWPM decoder [23]. Highlighted regions indicate uncertainty propagated from the standard error of the line-fit parameters of Fig. 6.

unrotated code for the same qubit count, and that this difference increases the larger the qubit count.

The ratio of the number of qubits used by each code to achieve the same  $p_L$  is displayed in Fig. 7. This is calculated using qubits counts from the line fits in Fig. 6. Additionally, the limit as  $p_L \rightarrow 0$  is indicated in Fig. 7 with an arrowhead for each  $p$ . These projections indicate that there is never a point for which the unrotated code’s qubit use becomes more efficient than the rotated code to achieve the same  $p_L$ . Exact qubit numbers for  $p_L = 10^{-12}$  are presented in the next section.

### D. Teraquops

A  $p_L$  per  $d$  rounds of  $p_L = 10^{-12}$  is known as the teraquop regime, so called as it implies a trillion logical operations (each requiring  $d$  rounds of stabiliser measurements) can be performed before, on average, one logical error occurs [27]. We calculated the qubits required to achieve this particular  $p_L$  using the least-squares line fits from Fig. 6. Fig. 8 shows the teraquop qubit counts for the rotated and unrotated codes. To achieve the teraquop regime at  $p = 10^{-3}$ , the rotated code uses  $1405 \pm 13$  qubits whereas the unrotated code uses  $1919 \pm 19$  qubits. This corresponds to the rotated code using  $74 \pm 1.3\%$  the number of qubits as the unrotated. However, the

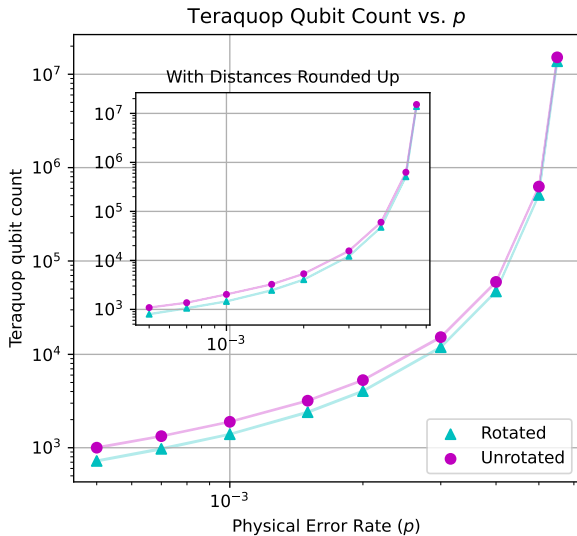


FIG. 8. Number of qubits needed to reach the teraquop regime (a  $p_L$  per  $d$  rounds of  $10^{-12}$ ). Inset displays qubit counts rounded up to the next code distance. Memory Z results are displayed but generalise to memory X (see Section II C). Teraquop qubit counts are calculated using weighted least-squares line fits from Fig. 6, with weights based on the root mean square error (RMSE) of the maximum likelihood estimates for  $p_L$ , assuming a binomial distribution. Line thickness indicates uncertainty, propagated from the standard errors of the line-fit parameters using these weights.

qubit counts calculated from the line-fits of Fig. 6 do not correspond to an exact distance. The inset in Fig. 8 displays qubit counts rounded up to the next achievable distance for each  $p$ . Using these rounded-up qubit counts, to achieve the teraquop regime at  $p = 10^{-3}$  the rotated code uses 1457 qubits ( $d = 27$ ) whereas the unrotated uses 2025 ( $d = 23$ ), corresponding to using 72% the number of qubits.

Very close to threshold the codes approach the same number of qubits counts. This corresponds with the regime close to threshold found by Beverland et al. [13] for the code capacity noise model where the unrotated code used less qubits than the rotated to achieve the same  $p_L$ . We found that under circuit-level noise this only occurs for the best-case unrotated code and at noise levels very close to threshold, namely above about  $p = 0.005$  (see appendix figures A.9,A.10,A.11). This region is much too close to threshold to be practical as it requires over 10 million physical qubits per logical qubit to achieve the teraquop regime. For all other physical error rates we can conclude that the rotated code uses less qubits to achieve a  $p_L$  of one in a trillion, and is hence the most efficient choice for performing useful quantum computation.

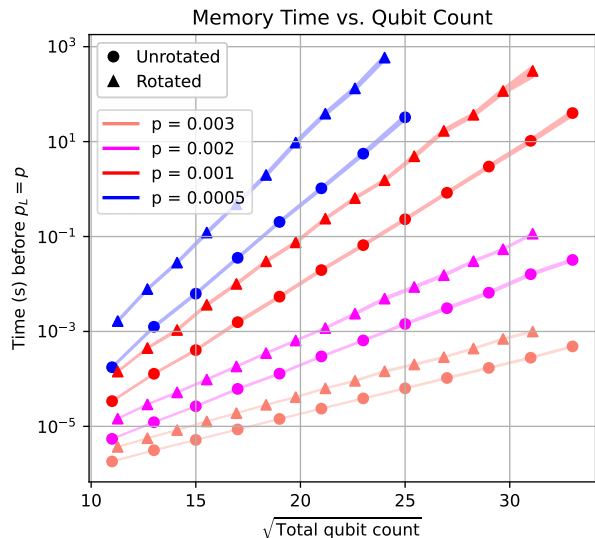


FIG. 9. The achievable memory times versus qubit count in the rotated or unrotated surface code for a selection of  $p$  values. This is the length of time a state can be encoded before a logical error is equally as likely as a physical error. Calculations of memory time assumes one round of stabiliser measurements takes one microsecond. Fig. presents memory Z results, which reproduce up to uncertainty for memory X (see Section IV A). Line thickness indicates uncertainty, calculated as the propagated RMSE of the MLEs for  $p_L$ , assuming a binomial distribution.

### E. Memory Times

For a given number of qubits we can compare the length of time a quantum memory employing either the rotated or unrotated surface code would last before the probability of a logical error is equal to that of a physical error. This is calculated as the number of rounds  $n_r$  that can be performed before  $p_L$  per  $n_r$  equals to  $p$ . We assume each round of stabiliser measurement takes a microsecond, the characteristic time in a superconducting quantum computer [39].

Fig. 9 displays the results for a selection of physical error rates for the rotated and unrotated surface codes. The rotated code achieves a higher memory time than the unrotated code for the same qubit count, indicating its applicability to procedures requiring quantum memory such as preserving quantum states when performing lattice surgery [9] or performing quantum communications with a quantum ‘sneakernet’ [40].

## V. CONCLUSION AND FURTHER WORK

Our work showed that the rotated code uses  $74 \pm 1.3\%$  the number of qubits used by the unrotated surface code to achieve a logical error rate of  $p_L = 10^{-12}$  at a physical error rate of  $p = 10^{-3}$  under uniform depolarising

circuit-level noise. For all other physical error rates below threshold, the ratio remains  $\sim 75\%$ , with the rotated code always outperforming the unrotated code even as  $p_L \rightarrow 0$ , as shown in Fig. 7. These results apply to both odd and even distances and were derived using the uncorrelated MWPM decoder Pymatching 2 [23]. We tested the assumption that because the rotated code uses less qubits to achieve the same distance as the unrotated, it should also use less qubits to achieve the same  $p_L$ , and continue to do so for high distances and low  $p_L$ . We confirmed that this is the case, and quantified the saving, with the exact ratio depending on the exact  $p$  and  $p_L$ . Our findings justify the use of the rotated code for further applications of the surface code.

Future work could look at noise models more representative of particular hardware, such as the superconducting inspired noise model of references [27, 41, 42]. This noise model reflects that reset and measurement take much longer than single and two-qubit gates in superconductors, with exact error probabilities detailed in [27]. As a preliminary investigation we implemented these error probabilities, but on circuits compiled with CNOT gates rather than CZ gates. These results can be found in appendix figures A.12 and A.13. There is a slight increase in teraquop qubit counts for both codes which slightly altered the ratio between them, however the ratios are similar to those for uniform depolarising circuit-level noise inasmuch as they roughly lie between 70 and 80%. Finding a more precise qubit saving ratios for this noise model would require more investigation, but preferably with circuits compiled with gates more applicable to superconductors such as CZ gates or iSWAP gates as the latter are native to superconductors and compiling circuits with them has been shown to reduce hardware overheads [42]. A further hardware overhead reduction could also be achieved by reducing stabiliser measurement circuits to a single step, rather than having them comprise numerous gates [43].

The mechanism which led to a best-case and worst-case unrotated code could be useful to explore if it also affects the rotated code in some way not revealed by our investigation. For the unrotated code, we did not see enough of an advantage gained from exploiting the asymmetry to warrant its use over the rotated, especially when considering other noise models such as biased noise. Biased noise is a notable case in which the rotated code outperforms the unrotated, even at the same distance, as shown by Tuckett et al. using the code capacity [44] and phenomenological [45] noise models.

While our work suggests a binary choice between the rotated or unrotated code, future work could explore surface codes with qubit numbers somewhere between these choices. While adding more qubits to a rotated code's lattice until it forms an unrotated code reduces the resulting  $p_L$  even without increasing the distance, it could follow that adding more qubits, even without adding enough to form the equivalent unrotated code, would also reduce  $p_L$ . The inverse has already been shown, namely that

using less qubits slightly increases  $p_L$ , specifically when re-using auxiliaries to measure boundary stabilisers [32]. We could expect then that adding slightly more qubits would slightly decrease  $p_L$ , and future work could look at quantifying the advantage of doing so. This would be relevant when considering that the number of qubits on a fabricated quantum computing device would usually not exactly correspond to a precise distance of a surface code. The caveat to this is that if the noise is highly biased, adding more qubits until the rotated code more closely resembles the unrotated could decrease performance, because under biased noise an unrotated code performs worse than a rotated for the same distance [44].

The effect of different decoders on the unrotated and rotated surface code could also be investigated. While [12] showed that a correlated decoder reduces  $p_L$  for both the rotated and unrotated surface code when compared to a decoder that did not take into account correlated errors, it was not quantified whether this reduction affected the rotated and unrotated codes equally. In our work we only implemented the sparse blossom algorithm of the PyMatching 2 decoder [23] which is not a correlated decoder. Future work could look at whether a correlated decoder, as well as other types of decoders such as maximum likelihood [46] or neural network decoders, affect these surface code types differently and affect their relative overheads.

Our work was a comparative study to provide numerical justification for the use of the rotated rather than the unrotated surface code as well as investigate the assumption that it is advantageous for very low logical error rates at high odd and even code distances. We ran numerical simulations to test its qubit saving when compared to the unrotated code not in achieving the same distance, but in achieving the same logical error rate, and showed using projections of the numerical simulations that this saving continues for arbitrarily high distances and consequently low logical error rates. We did so using uniform depolarising circuit-level noise and the MWPM decoder PyMatching 2 [23] and can conclude that under these conditions and at an operational physical error rate of  $p = 10^{-3}$  the rotated surface code uses around 74% the number of qubits used by the unrotated code.

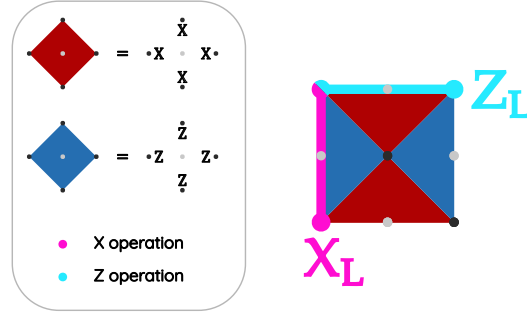
## ACKNOWLEDGMENTS

We thank Craig Gidney for valuable discussions and suggesting CNOT order as the cause of the asymmetry in the unrotated code's performance. We thank Alan Robertson, Michael Newman and Ben Criger for valuable discussions. This research received funding from the Defense Advanced Research Projects Agency Quantum Benchmarking program under Award No. HR00112230007 and HR001121S0026 contracts. We acknowledge the traditional owners of the land on which this work was undertaken at the University of Technology Sydney: the Gadigal people of the Eora Nation.

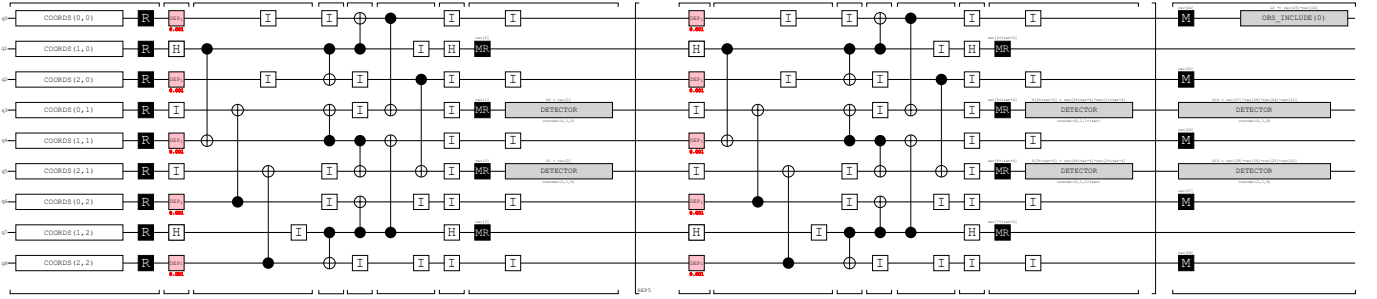
- 
- [1] P. W. Shor, Polynomial-time algorithms for prime factorization and discrete logarithms on a quantum computer, *SIAM J.Sci.Statist.Comput.* **26** (1997) 1484 **quant-ph**, 10.1137/S0097539795293172 (1995).
- [2] I. M. Georgescu, S. Ashhab, and F. Nori, Quantum simulation, *Rev. Mod. Phys.* **86**, 154 (2014) **quant-ph**, 10.1103/RevModPhys.86.153 (2013).
- [3] D. Gottesman, *Stabilizer codes and quantum error correction* (California Institute of Technology, 1997).
- [4] A. Steane, Active stabilization, quantum computation, and quantum state synthesis, *Physical Review Letters* (1997).
- [5] S. J. Devitt, W. J. Munro, and K. Nemoto, Quantum error correction for beginners, *Reports on Progress in Physics* **76**, 076001 (2013).
- [6] A. Y. Kitaev, Fault tolerant quantum computation by anyons, *Annals of Physics* **303**, 2 (1997).
- [7] A. M. Stephens, Fault-tolerant thresholds for quantum error correction with the surface code, *Physical Review A* **89**, 022321 (2014).
- [8] R. Acharya, L. Aghababaie-Beni, I. Aleiner, T. I. Andersen, M. Ansmann, F. Arute, K. Arya, A. Asfaw, N. Astrakhantsev, J. Atalaya, *et al.*, Quantum error correction below the surface code threshold, *arXiv preprint arXiv:2408.13687* (2024).
- [9] C. Horsman, A. G. Fowler, S. Devitt, and R. Van Meter, Surface code quantum computing by lattice surgery, *New Journal of Physics* **14**, 123011 (2012).
- [10] H. Bombin and M. Martin-Delgado, Optimal resources for topological two-dimensional stabilizer codes: Comparative study, *Physical Review A* **76**, 012305 (2007).
- [11] S. B. Bravyi and A. Y. Kitaev, Quantum codes on a lattice with boundary, *arXiv preprint quant-ph/9811052* (1998).
- [12] A. Paler and A. Fowler, Pipelined correlated minimum weight perfect matching of the surface code, *Quantum* **2023**, 1205 (2022).
- [13] M. E. Beverland, B. J. Brown, M. J. Kastoryano, and Q. Marolleau, The role of entropy in topological quantum error correction, *Journal of Statistical Mechanics: Theory and Experiment* **2019**, 073404 (2019).
- [14] B. Criger and I. Ashraf, Multi-path summation for decoding 2d topological codes, *Quantum* **2**, 102 (2018).
- [15] B. M. Terhal, Quantum error correction for quantum memories, *Reviews of Modern Physics* **87**, 307 (2015).
- [16] L. Skoric, D. E. Browne, K. M. Barnes, N. I. Gillespie, and E. T. Campbell, Parallel window decoding enables scalable fault tolerant quantum computation, *Nature Communications* **14**, 7040 (2023).
- [17] S. Bravyi, M. Suchara, and A. Vargo, Efficient algorithms for maximum likelihood decoding in the surface code, *Physical Review A* **90**, 032326 (2014).
- [18] D. Bacon, S. T. Flammia, A. W. Harrow, and J. Shi, Sparse quantum codes from quantum circuits, *IEEE Transactions on Information Theory* **63**, 2464 (2017).
- [19] E. Dennis, A. Kitaev, A. Landahl, and J. Preskill, Topological quantum memory, *Journal of Mathematical Physics* **43**, 4452 (2002).
- [20] A. G. Fowler, Minimum weight perfect matching of fault-tolerant topological quantum error correction in average  $o(1)$  parallel time, *arXiv preprint arXiv:1307.1740* (2013).
- [21] N. Delfosse and N. H. Nickerson, Almost-linear time decoding algorithm for topological codes, *Quantum* **5**, 595 (2021).
- [22] S. Huang, M. Newman, and K. R. Brown, Fault-tolerant weighted union-find decoding on the toric code, *Physical Review A* **102**, 012419 (2020).
- [23] O. Higgott and C. Gidney, Sparse blossom: correcting a million errors per core second with minimum-weight matching, *arXiv preprint arXiv:2303.15933* (2023).
- [24] Y. Wu and L. Zhong, Fusion blossom: Fast mwpm decoders for qec, in *2023 IEEE International Conference on Quantum Computing and Engineering (QCE)*, Vol. 1 (IEEE, 2023) pp. 928–938.
- [25] N. Liyanage, Y. Wu, A. Deters, and L. Zhong, Scalable quantum error correction for surface codes using fpga, in *2023 IEEE International Conference on Quantum Computing and Engineering (QCE)*, Vol. 1 (IEEE, 2023) pp. 916–927.
- [26] O. Higgott, T. C. Bohdanowicz, A. Kubica, S. T. Flammia, and E. T. Campbell, Improved decoding of circuit noise and fragile boundaries of tailored surface codes, *Physical Review X* **13**, 031007 (2023).
- [27] C. Gidney, M. Newman, A. Fowler, and M. Broughton, A fault-tolerant honeycomb memory, *Quantum* **5**, 605 (2021).
- [28] G. Q. AI, Suppressing quantum errors by scaling a surface code logical qubit, *Nature* **614**, 676 (2023).
- [29] J. Preskill, Reliable quantum computers, *Proceedings of the Royal Society of London. Series A: Mathematical, Physical and Engineering Sciences* **454**, 385 (1998).
- [30] A. G. Fowler, M. Mariantoni, J. M. Martinis, and A. N. Cleland, Surface codes: Towards practical large-scale quantum computation, *Physical Review A* **86**, 032324 (2012).
- [31] A. Fowler, A. M. Stephens, and P. Groszkowski, High-threshold universal quantum computation on the surface code, *Phys. Rev. A* **80**, 10.1103/PhysRevA.80.052312 (2009).
- [32] Y. Tomita and K. M. Svore, Low-distance surface codes under realistic quantum noise, *Physical Review A* **90**, 062320 (2014).
- [33] M. B. Hastings and J. Haah, Dynamically generated logical qubits, *Quantum* **5**, 564 (2021).
- [34] C. Gidney, Stim: a fast stabilizer circuit simulator, *Quantum* (2021a).
- [35] C. Gidney, Sinter source code, <https://github.com/quantumlib/Stim/tree/main/glue/sample> (2022), accessed: 20 11 2023.
- [36] C. Gidney, The stim circuit file format (.stim), [https://github.com/quantumlib/Stim/blob/main/doc/file\\_format\\_stim\\_circuit.md](https://github.com/quantumlib/Stim/blob/main/doc/file_format_stim_circuit.md) (2024).
- [37] O. Higgott and F.-M. Le Régent, Stimcircuits, <https://github.com/oscarhiggott/StimCircuits> (2024).
- [38] C. Gidney, Inbuilt stim circuits showing unexpected memory x and memory z logical error rates for unrotated surface code, StackExchange answer in <https://quantumcomputing.stackexchange.com/questions/32941/inbuilt-stim-circuits-showing-unexpected-memory-x-and-memory-z-logical-error-rat/32959#32959> (2023), accessed: 2024-03-06.

- [39] S. Saadatmand, T. L. Wilson, M. Field, M. K. Vijayan, T. P. Le, J. Ruh, A. S. Maan, I. Moflic, A. Caesura, A. Paler, *et al.*, Fault-tolerant resource estimation using graph-state compilation on a modular superconducting architecture, arXiv preprint arXiv:2406.06015 (2024).
- [40] S. J. Devitt, A. D. Greentree, A. M. Stephens, and R. Van Meter, High-speed quantum networking by ship, *Scientific reports* **6**, 36163 (2016).
- [41] C. Gidney, M. Newman, and M. McEwen, Benchmarking the planar honeycomb code, *Quantum* **6**, 813 (2022).
- [42] M. McEwen, D. Bacon, and C. Gidney, Relaxing hardware requirements for surface code circuits using time-dynamics, arXiv preprint arXiv:2302.02192 (2023).
- [43] G. Üstün, A. Morello, and S. Devitt, Single-step parity check gate set for quantum error correction, *Quantum Science and Technology* **9**, 035037 (2024).
- [44] D. K. Tuckett, A. S. Darmawan, C. T. Chubb, S. Bravyi, S. D. Bartlett, and S. T. Flammia, Tailoring surface codes for highly biased noise, *Physical Review X* **9**, 041031 (2019).
- [45] D. K. Tuckett, S. D. Bartlett, S. T. Flammia, and B. J. Brown, Fault-tolerant thresholds for the surface code in excess of 5% under biased noise, *Physical review letters* **124**, 130501 (2020).
- [46] E. Dennis, A. Kitaev, A. Landahl, and J. Preskill, Topological quantum memory, *Journal of Mathematical Physics* **43**, 4452 (2002).

## Appendix: Supplementary Figures



(a)



(b)

FIG. A.1. Subfigure (a) shows two possible logical operators and the stabiliser arrangement for a distance 2, unrotated surface code. Subfigure (b) shows the ‘timeline-svg’ generated by Stim [34] of our circuit file realising a memory Z experiment on the distance-2 unrotated surface. It uses 21302130 CNOT order. All gates are faulty as per Section III. Also depicted is the depolarising errors applied on data qubits before each round of stabiliser measurements. For this example  $p = 10^{-3}$ . Time steps are indicated with horizontal square brackets. The repeated section is indicated with vertical square brackets. R implies reset to  $|0\rangle$ , I is the identity gate (an idling error), CNOT gates are marked as usual from control to target. MR is a sequential combination of a measure and reset gate in the Z basis. Both the measurement and the reset can be faulty. Detectors create the matching graph from stabiliser measurement results to be given to PyMatching, and the included observable is a calculation of the state of the measured logical observable based on the measurement results of the data qubits.

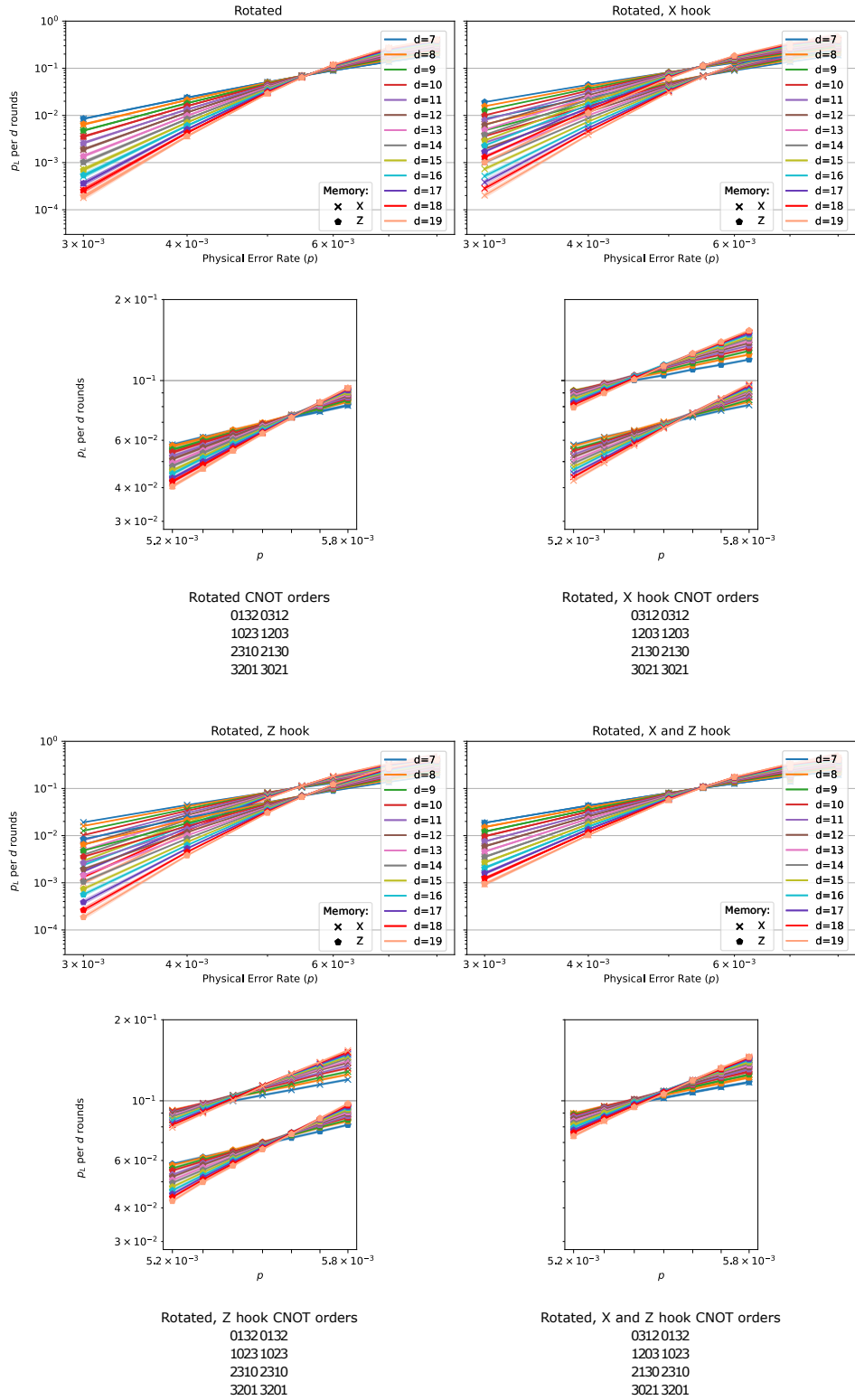


FIG. A.2. Rotated surface code plots of  $p_L$  versus  $p$  from monte carlo sampling of simulated memory experiments using all valid (see Section II C) CNOT orders, including with hook errors. Lower plots show zoomed-in regions of the upper plots with additional data points. The numbering used to designate CNOT order is explained in Fig. 2. Listed CNOT orders give identical plots up to uncertainty so are grouped. X (Z) hook errors (Section II C) reduce the number of single physical errors required to form an  $X_L$  ( $Z_L$ ) logical operator so increase the  $p_L$  and decrease the threshold when preserving the  $|0\rangle_L$  ( $|+\rangle_L$ ) state, corresponding to Memory Z (Memory X).

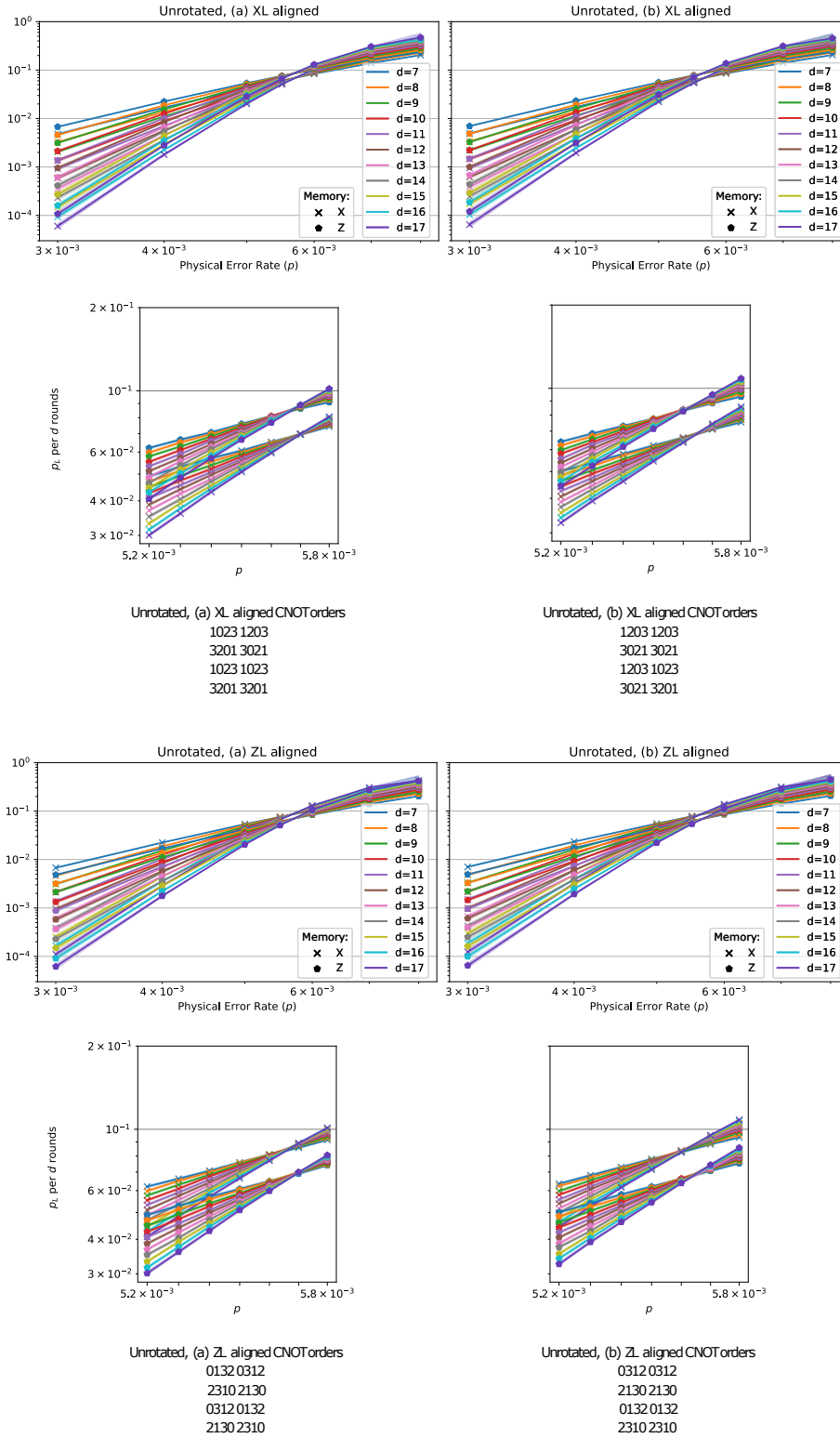


FIG. A.3. Unrotated surface code plots of  $p_L$  versus  $p$  from monte carlo sampling of simulated memory experiments using all valid (see Section II C) CNOT orders. Lower plots show zoomed-in regions of the upper plots with additional data points. The numbering used to designate CNOT order is explained in Fig. 2. Listed CNOT orders give identical plots up to uncertainty so are grouped. The second and third CNOT gates aligning with  $Z_L$  ( $X_L$ ) correlates with reduced performance in Memory X (Z) (see Section IV A). Additionally, (a) CNOT orders slightly outperform (b) CNOT orders, having a marginally higher threshold and lower  $p_L$ . These do not correspond to hook-error orders in the rotated code.

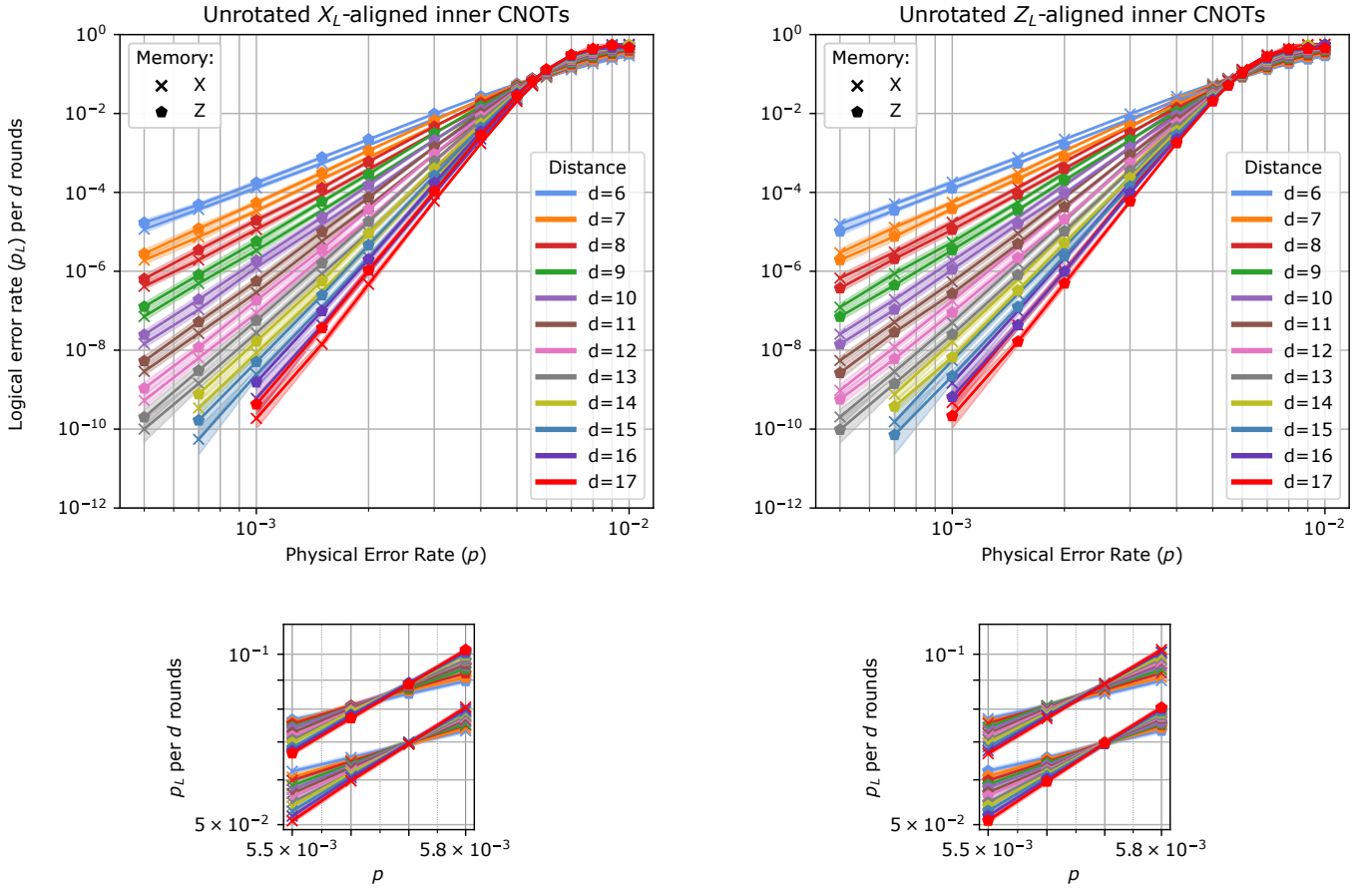


FIG. A.4. Comparing the  $X_L$ -aligned inner CNOT unrotated surface code to the  $Z_L$ -aligned inner CNOT unrotated surface code. We see that their memory X and Z results invert and that the worst-case and best-case codes in each memory type are identical up to uncertainty. The  $Z_L$ -aligned plot is a repeat of the plot in the main text (Fig. 5) included for comparison. These graphs plot logical error rate ( $p_L$ ) per  $d$  rounds of stabiliser measurements versus physical error rate ( $p$ ) of uniform depolarising circuit-level noise from monte carlo sampling of numerical simulations in unrotated surface code. Memory X (Z) preserves the  $|0\rangle_L$  ( $|+\rangle_L$ ) state. The threshold ( $p_{th}$ ) is the  $p$  value below which increasing the code distance decreases  $p_L$ , i.e. where the curves intersect. Lower plots show a zoomed-in region close to  $p_{th}$  with additional simulated data points. The unrotated code shows a split in  $p_L$  between memory types depending on CNOT gate order. This was despite simulations for both codes having effectively equal depth stabiliser measurement circuits. If the second and third CNOT gates (out of the four per stabiliser measurement circuit) were aligned with  $Z_L$  ( $X_L$ ) the  $p_L$  for memory X (Z) increased. This reproduced in all valid CNOT orders (see Appendix Fig. A.3). Highlighted regions show  $p_L$  values for which the conditional probabilities  $P(p_L|k)$  are within a factor of 1000 of the MLE  $p_L = k/n$ , assuming a binomial distribution. While the results from these CNOT orders generalise (see Section IV A), for specificity they are 10231203 for  $X_L$ -aligned and 23102130 for  $Z_L$ -aligned, using the numbering described in Fig. 2.

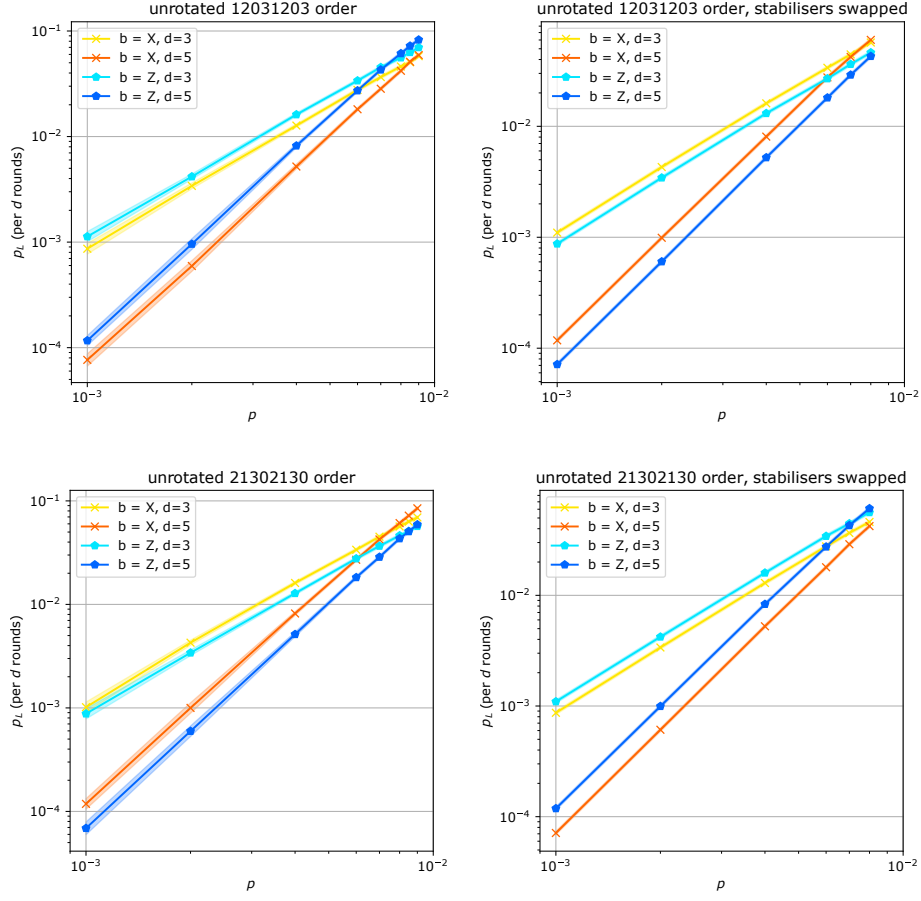


FIG. A.5. Investigation of the effect on the unrotated code of inverting the stabilisers. This was to rule out the observed CNOT order affect on the unrotated code, discussed in Section IV A, being artificially introduced by Stim or PyMatching from the way we chose to orientate our code, namely with  $X_L$  being a vertical chain and  $Z_L$  a horizontal. Inverting the stabilisers effectively rotates the matching graph given to PyMatching by ninety degrees. The graphs on the left show the usual orientations, the graphs on the right show the orientations with the stabilisers swapped.  $X_L$ -aligned inner CNOTs become  $Z_L$ -aligned inner CNOTs and vice versa when the stabilisers are swapped, and this is reflected in the perfect inversion (up to uncertainty) between the memory X and memory Z performance. This indicates that is not an artificial affect from, for example, a possible bias in decoding in matching along a particular orientation. Note that to isolate the effect of CNOT alignment on the unrotated code these simulations were run using equal depth stabiliser-extraction circuits but without idling errors, which is inconsistent with the other results in this paper. Consequently, the exact quantities for  $p$  and  $p_L$  can be compared between plots in this figure but should not be compared to other plots in the paper which *do* simulate idling errors.

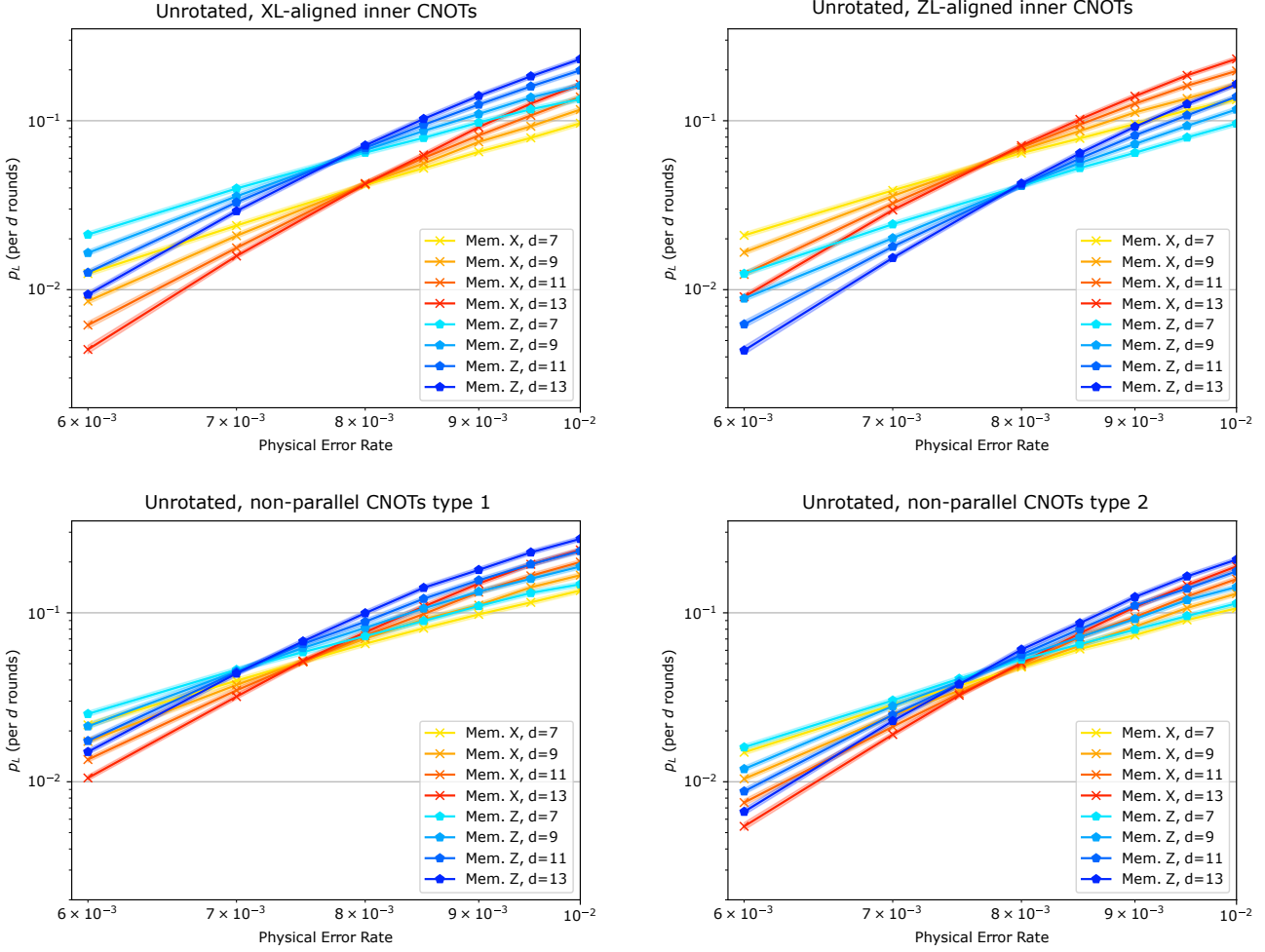


FIG. A.6. Investigation of the effect on the unrotated code of using CNOT orders in the stabiliser measurement circuits which intersperse CNOT alignment between  $X_L$  and  $Z_L$  (and as a consequence feature non-parallel alignment of CNOTs, see Section II C). The top two graphs feature usual CNOT orders so are just for comparison. They show the inversion noted in the main text (Section IV A) in performance between Memory X and Memory Z which correlates with the inner CNOTs of the stabiliser extraction circuits being aligned with  $Z_L$  and  $X_L$  respectively. If this inner CNOT alignment was a causative effect we would expect interspersing the CNOT alignments, as was done in the lower two plots, to balance out the effect. However, we see an overall increase in  $p_L$  when we do this, as shown in the lower two figures. Additionally, Memory Z then consistently had a higher  $p_L$  for these CNOT orders. The CNOT orders which we refer to as ‘type 1’ resulted in the plot in the lower left. These were 01321023, 01231032, 10230132 and 10320123. The lower right plot was for ‘type 2’ orders 02131302 and 13020213. Note that to isolate the effect of CNOT alignment on the unrotated code these simulations were run using equal depth stabiliser-extraction circuits but without idling errors, which is inconsistent with the other results in this paper. Consequently, the exact quantities for  $p$  and  $p_L$  can be compared between plots in this figure but should not be compared to other plots in the paper which *do* simulate idling errors.

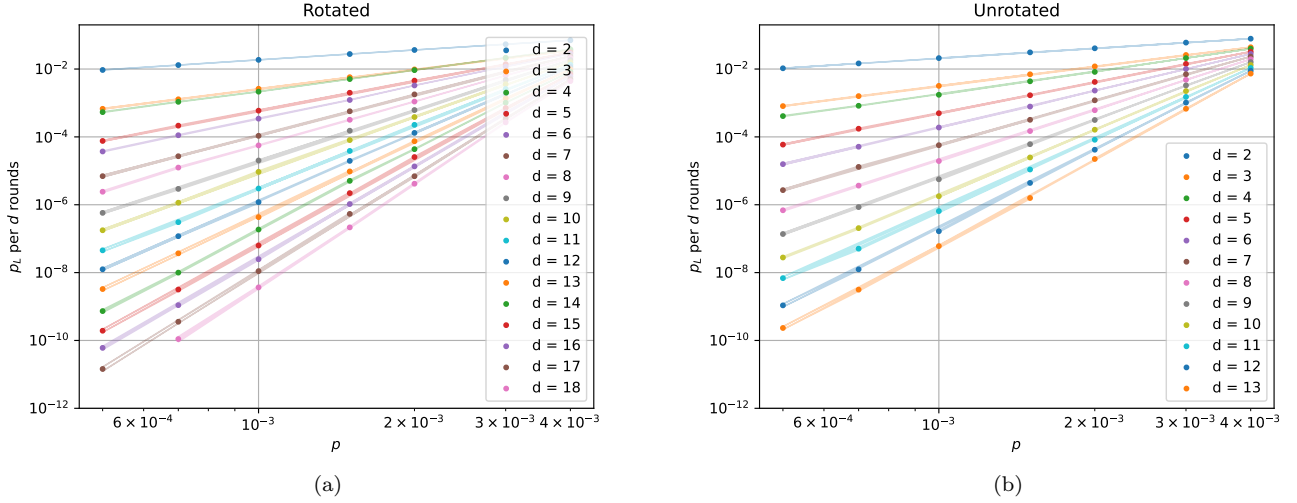


FIG. A.7. Plots showing the  $p_L$  vs.  $p$  for the rotated and unrotated surface codes including lower-distance codes than presented in the main text. Plots present the same data as Fig. 5 but for  $d = 2$  to  $d = 18$  ( $n = 647$ ) for the rotated code and  $d = 2$  to  $d = 13$  ( $n = 625$ ) for the unrotated code. We note that low-distance codes do not fit the scaling relationships of higher-distance codes and that there is a marked difference between the scaling relationship of odd and even codes at low distances but this diminishes at higher distances. Plots show memory Z and worst-case unrotated surface code but these results are identical up to uncertainty for memory X (see Appendix Fig. A.4). Highlighted regions indicate uncertainty from Monte Carlo sampling. They show the RMSE of the maximum likelihood estimate for  $p_L$  assuming a binomial distribution.

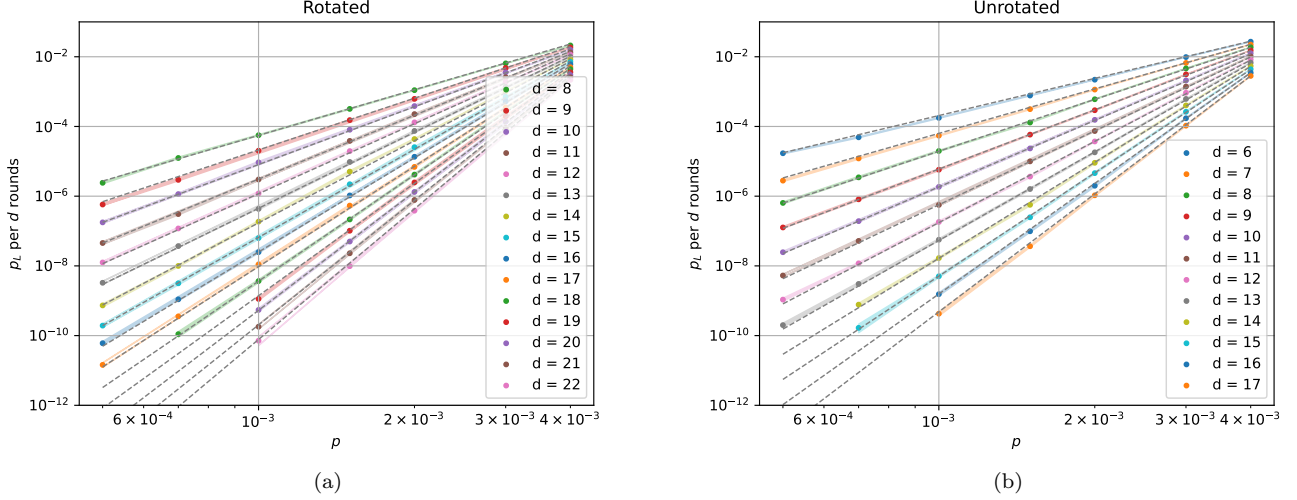


FIG. A.8. Function fit plots showing the fitted function  $p_L = \alpha(p/\beta)^{\gamma d - \delta}$  as grey dashed lines with parameters for combined odd and even distances as per Table III. These plots display the same data as Fig. 5 but with the function fits overlaid, for physical error rates  $p < 0.004$  and with the highlighted uncertainty regions instead being the RMSE of the maximum likelihood estimate for  $p_L$ . As in Fig. 5, these plots show memory Z and worst-case unrotated surface code but these are identical up to uncertainty for memory X (see Appendix Fig. A.4).

Code	Distances	$\alpha$	$\beta$	$\gamma$	$\delta$
Rotated	Odd	$0.081 \pm 0.014$	$0.00531 \pm 0.00002$	$0.577 \pm 0.010$	$0.24 \pm 0.16$
	Even	$0.077 \pm 0.012$	$0.00528 \pm 0.00003$	$0.579 \pm 0.006$	$0.30 \pm 0.10$
	Combined	$0.078 \pm 0.009$	$0.00529 \pm 0.00003$	$0.578 \pm 0.006$	$0.27 \pm 0.09$
Unrotated	Odd	$0.084 \pm 0.011$	$0.00542 \pm 0.00001$	$0.701 \pm 0.013$	$0.66 \pm 0.17$
	Even	$0.078 \pm 0.012$	$0.00537 \pm 0.00002$	$0.698 \pm 0.011$	$0.64 \pm 0.12$
	Combined	$0.080 \pm 0.008$	$0.00539 \pm 0.00002$	$0.700 \pm 0.008$	$0.65 \pm 0.10$

TABLE III. Fits to  $p_L = \alpha(p/\beta)^{\gamma d - \delta}$  (Equation 4) using  $d \geq 6$  (8) for the unrotated (rotated) code and  $p \leq 0.004$ . The parameters for the combined (both odd and even) fits are quoted in the main text (Section IV B) because the results for odd and even distances are identical up to uncertainty. Plots with these fits overlaid on the simulated data are shown in Appendix Fig. A.8. Line fits were performed on each distance's  $p_L$  versus  $p$  curve for  $p \leq 0.004$  and  $\beta$  is the  $p$  value of the closest point to all the lines, with its uncertainty being the maximum of the perpendicular distance to each line. The standard errors in the line-fit parameters for each distance were used to perform a weighted average to calculate  $\alpha$  and its uncertainty. The best  $\gamma$  and  $\delta$  were calculated from using each distance's line-fit gradient,  $m$ , and fitting to  $m = \gamma d + \delta$ . The standard error in these parameters is the square root of the sum of the residual variance and the the mean of the variance of each  $m$ .

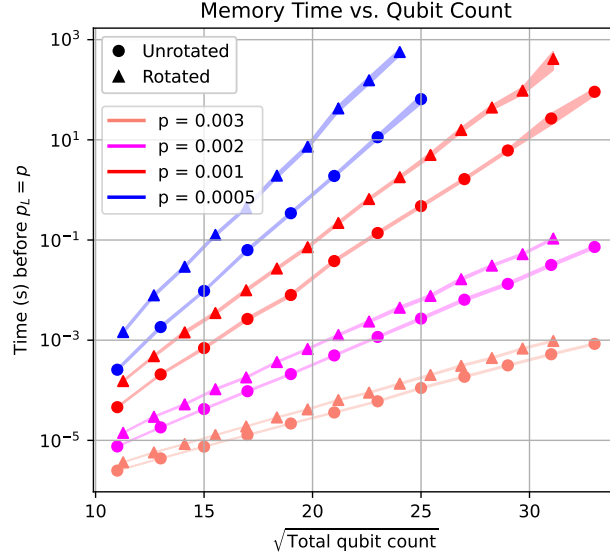


FIG. A.10. The achievable memory times versus qubit count in the rotated and best-case unrotated surface code. This is the length of time a state can be encoded before a logical error is equally as likely as a physical error. Calculations of memory time assume one round of stabiliser measurements takes one microsecond. Fig. presents memory X results. Line thickness indicates uncertainty, calculated as the propagated RMSE of the MLEs for  $p_L$ , assuming a binomial distribution.

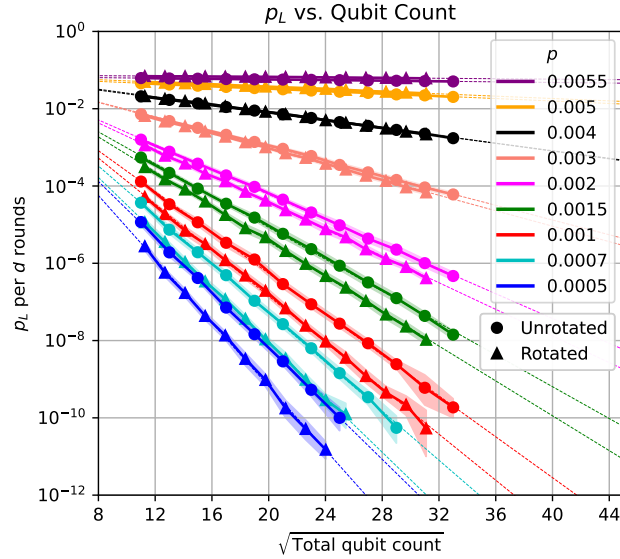


FIG. A.9. Line-fit plot projecting  $p_L$  as a function of qubit count at various physical error rates for the rotated and best-case unrotated surface code. We see that the best-case unrotated surface code uses less qubits than the rotated for high  $p$  very close to threshold, but at this  $p$  the qubit numbers are intractable. We fit to  $d \geq 8$  for the rotated and  $d \geq 6$  for the unrotated code to minimise edge effects. The points of intersection between these least-squares line fits and  $p_L = 10^{-12}$  are used to generate the teraquop plot in Appendix Fig. A.11. Highlighted regions show  $p_L$  values for which the conditional probabilities  $P(p_L|k)$  are within a factor of 1000 of the MLE  $p_L = k/n$ , assuming a binomial distribution. Fig. presents memory Z results but is identical up to uncertainty to memory X results when also using a best-case unrotated code CNOT ordering.

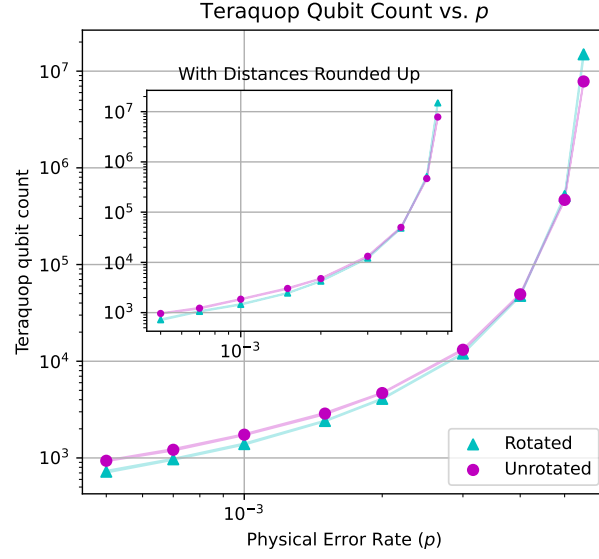


FIG. A.11. Number of qubits required to reach the teraquop regime (a  $p_L$  per  $d$  rounds of  $10^{-12}$ ) as a function of  $p$  for the rotated and best-case unrotated surface code. The inset displays qubit counts rounded up to the next achievable code distance and has some discretisation effects. Memory X results are displayed but generalise to best-case memory Z (see Section II C). Teraquop qubit counts are calculated using weighted least-squares line fits from Appendix Fig. A.9, with weights based on the RMSE of the MLEs for  $p_L$ , assuming a binomial distribution. Line thickness indicates uncertainty, propagated from the standard errors of the line-fit parameters using these weights.

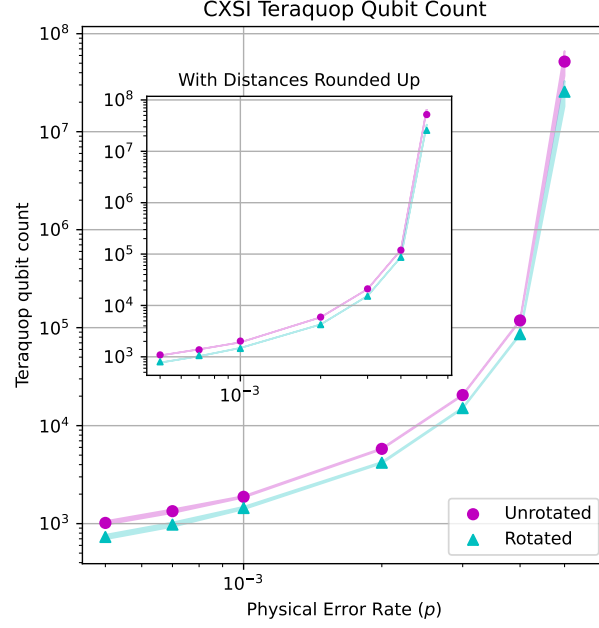


FIG. A.12. Teraquop qubit count, that is the number of physical qubits required for a  $p_L$  per  $d$  rounds of  $10^{-12}$ , versus physical error rate for the rotated and worst-case unrotated surface codes when implemented with circuits experiencing *superconducting inspired* noise but compiled with CNOT gates. We refer to this as CXSI. These simulations were conducted as a preliminary investigation into whether using the higher and more specific error probabilities of the ‘superconducting inspired’ noise model of references [27, 41, 42] could have different relative effects on the unrotated and rotated code and change the conclusion drawn from the uniform depolarising noise model. For specificity the rotated CNOT order here is 32013021 whereas the unrotated CNOT order is 12031203, but these results generalise to all valid (see Section II C) CNOT orders. We show results for memory Z and worst-case unrotated code. Memory X is identical up to uncertainty. The teraquop qubit count is calculated from line projections from simulation results and do not usually correspond to an exact distance in the surface codes. The inset shows the results rounded up to correspond to have the qubit count correspond to an exact distance. Line thickness indicates uncertainty, propagated from the standard errors of the line-fit parameters using weights based on the RMSE of the MLEs for  $p_L$ .

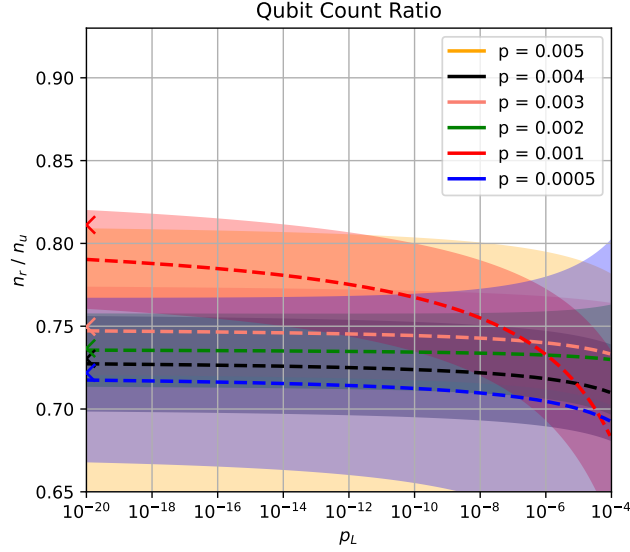


FIG. A.13. Results from a preliminary investigation of ‘CXSI’ noise (superconducting inspired circuits compiled with CNOT gates) showing the ratio of the number of qubits used by the rotated versus the unrotated surface code to achieve the same logical error rate ( $p_L$ ) per  $d$  rounds of stabiliser measurements. We note that the ratios are similar to those for uniform depolarising circuit-level noise presented in the main text inasmuch as they roughly lie between 70 and 80%. Further investigation of this noise model is necessary for more precise ratios. However, as noted in the main text, it would be more applicable to superconducting hardware to compile the circuits using iSWAP gates [42]. Qubit counts were calculated from the line-fits to each physical error rate’s  $p_L$  vs. qubit count. Coloured arrowheads on the y-axis indicate the limit as  $p_L \rightarrow 0$ . Simulations used an uncorrelated MWPM decoder [23]. Highlighted regions indicate uncertainty propagated from the standard error of the line-fit parameters, where lines were fit to the MLE of each  $p_L$  and weighted by the RMSE of each MLE.